analytical chemistry

pubs.acs.org/ac Article

Contactless Photoelectrochemical Biosensor Based on the Ultraviolet−Assisted Gas Sensing Interface of Three-Dimensional SnS_2 Nanosheets: From Mechanism Reveal to Practical Application

Lingting Huang,[ξ] Guoneng Cai,[ξ] Ruijin Zeng, Zhichao Yu, and Dianping Tang*

Cite This: *Anal. Chem.* 2022, 94, 9487−9495 Read Online

ACCESS | Metrics & More | Article Recommendations | Supporting Information

ABSTRACT: This work reports a contactless photoelectrochemical biosensor based on an ultraviolet-assisted gas sensor (UV−AGS) with a homemade three-dimensional (3D)-SnS_2 nanosheet-functionalized interdigitated electrode. After rigorous examination, it was found that the gas responsiveness accelerated and the sensitivity increased using the UV irradiation strategy. The effects of the interlayer structure and the Schottky heterojunction on the gas-sensitive response of O_2 and NH_3 under UV irradiation were further investigated theoretically by 3D electrostatic field simulations and first-principles density functional theory to reveal the mechanism. Finally, a UV−AGS device was developed to quantify the blood ammonia bioassay in a small-volume whole blood sample by alkalizing blood to release gas-phase ammonia with a linear range of 25−5000 μM with a limit of detection (LOD) of 29.5 μM. The device also enables a rapid immunoassay of human cardiac troponin I (cTnI) with a linear range of 0.4−25.6 ng/mL and an LOD of 0.37 ng/mL using a urease-labeled antibody as the immune recognition molecule. Both analyses showed satisfying specificity and stability, suggesting that the device can be applied to practical assays and is of great potential to increase the value of gas-sensitive sensors in chemical biosensing.

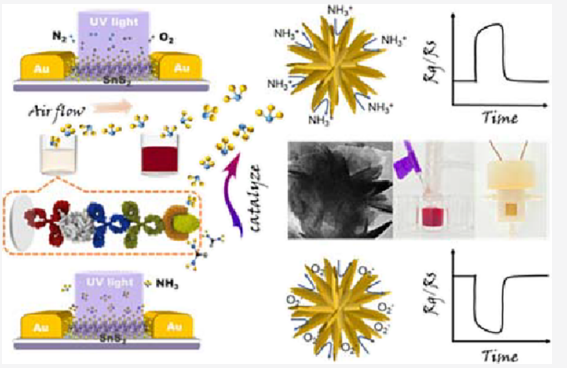

Research on photoelectrochemical biosensors is of great interest and has generated very active research communities in food security analysis, medical research, disease diagnosis, and environmental monitoring in recent years with unique technical advantages in terms of high sensitivity, low cost, and simplicity.[1−3] However, one of the inevitable key difficulties remains poorly addressed as the electrode interface relies on the electroactive material in solution and tends to delaminate and deactivate with repeated use.[4,5] Similar to photoelectrochemical sensors, electrically transduced gas sensors emit an electrical response signal, which in principle undergoes a change in the conductivity of the semiconductor (mostly metal oxides) interface when it comes into contact with the target gas.[6,7] However, to achieve good sensor performance, the temperature required by the gas sensing working interface needs to generally be higher than room temperature, which limits its development, especially in the field of biosensing. Notably, some semiconductors also have photoelectric conversion capabilities, meaning that a large number of photogenerated carriers can be generated upon irradiation with specific wavelengths to facilitate the adsorption and desorption of the target gas molecules.[8,9] Hence, the introduction of illumination is also considered as one of the strategies to improve the performance of gas sensors. It is promisingly assumed that the selection of gas-sensing functionalized photoelectronic semiconductors to construct a light-assisted sensing interface is the key to increasing the value of gas sensors in the field of biosensing and also provides a solution strategy for building non-contact photoelectrochemical biosensors.

Monolayer SnS_2 is an n-type semiconductor with a high on/off current ratio (~10^6) and carrier mobility (~230 $cm^2/V\cdot s$),[10,11] which can be used in a wide range of electronic devices, including field-effect transistors (FETs),[12] photodetection,[13] thermoelectric devices,[14] and various types of gas sensors.[15,16] The sizable band gap (1.82−2.41 eV) possessed by SnS_2, used in gas sensing, facilitates the formation of adsorbed states on the surface by gas molecules, effectively modifying its electrical properties.[17] Nevertheless, the carrier concentration generated by monolayer SnS_2 NSs alone is limited to a weak electrical current (~nA) generated by changing the Schottky barrier, resulting in the terminal output requiring a sensitive and inconvenient electrochemical workstation. Remarkably, three-

Received: May 8, 2022
Accepted: June 10, 2022
Published: June 23, 2022

https://doi.org/10.1021/acs.analchem.2c02010
Anal. Chem. 2022, 94, 9487−9495

dimensional nanosheet aggregates (3D-SnS_2 NSs) composed of SnS_2 NSs can be synthesized in large quantities by simple solvothermal treatments or water-bath deposition methods and are therefore widely used as catalysts in photocatalytic reactions because of their improved properties, amount of charge carriers per unit space, and a sufficient number of active sites.[18−20] Ascribed to the advantages offered, gas sensors developed on the basis of 3D-SnS_2 NSs have been reported.[18,21] However, there are still some unclear concerns that need to be addressed. (i) Mutual superimposition of nanosheets introduces interface potential barriers (surface states with adsorbed oxygen) in SnS_2−SnS_2. (ii) The adsorption sites within the gap structure are initially occupied by adsorbed-O_2, which is not conducive to the adsorption and desorption of the measured gas molecules. The above deficiencies lead to an increased response signal, accompanied by a decrease in sensitivity and a more time-consuming response-recover process. The usual solution is to increase the operating temperature, but this significantly increases the material loss and equipment energy consumption, which is inappropriate for daily detection. Another approach is to directly use ultraviolet (UV) irradiation onto the sensing interface to create photogenerated holes/carriers, which can significantly increase the adsorption and desorption rate of gas molecules at room temperature.[22] Meanwhile, UV-assisted gas sensing systems are even more rarely used because the mechanism is still unclear and the signal easily be disturbed. Therefore, choosing an appropriate gas-sensitive enhancement strategy based on those discussed above is the key to expanding the application scenario of gas-sensing devices.

Abnormally elevated levels of free ammonia in human blood (blood ammonia) can cause hyperammonemia, which may lead to delirium, brain damage, and even death. The development of the rapid detection of blood ammonia in small-volume whole blood samples has been a hot topic in bioanalysis.[23,24] On the other hand, as one of the specific markers of acute myocardial infarction (AMI),[25] this is of particular importance for the sensitive detection of human cardiac troponin I (cTnI) in a short time. Based on the above contents, as a proof of concept, this work presents a contactless photoelectrochemical biosensor based on 3D-SnS_2 NSs with a UV-assisted gas-phase detection system for blood ammonia and cTnI detection (Scheme 1). In brief, 3D-SnS_2 NSs are prepared by a water bath deposition method and further deposited onto interdigitated electrodes (IDEs) using a spin-coating method to form 3D-SnS_2 NSs/IDEs. With further verifying the gas-sensitive properties, the working mechanism within the effects of UV irradiation, the structure of 3D-SnS_2 NSs, and the Schottky barrier between Au and SnS_2 heterojunction on the gas-sensitive response of O_2 and NH_3 are systematically understood by three-dimensional electrostatic field simulations and first-principles density functional theory (DFT) calculations. According to this principle, an ultraviolet-assisted gas sensor (UV−AGS) device is designed to detect free ammonia in whole blood. To further demonstrate the broad applicability of this biosensor, a sandwich-type integrated gas-phase immunoassay is constructed for the quantitative analysis of human cTnI using a UV−AGS device as the signal readout and urease-labeled antibody as the immune recognition molecule.

Scheme 1. Schematic Illustration of the UV−AGS Device Based on 3D-SnS_2 NSs/IDEs for Blood Ammonia Analysis and the Gas-Phase Immunoassay

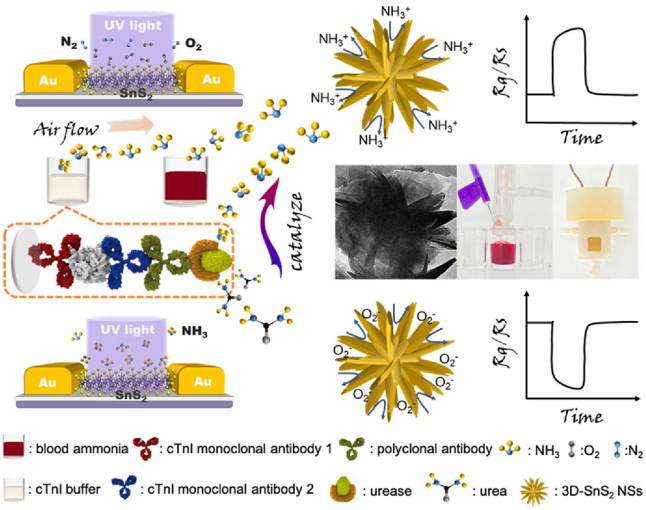

EXPERIMENTAL SECTION

Preparation of 3D-SnS_2 Nanosheets/Interdigitated Electrodes (3D-SnS_2 NSs/IDEs). The gas-sensing films based on 3D-SnS_2 NSs were prepared on gold-deposited Al_2O_3 ceramic IDEs by the spin coating technique. Initially, the IDE was soaked in acetone for 15 min, cleaned successively with ethanol and ultrapure water, and then dried in vacuum at 60 °C. Then, 5.0 mg of the prepared 3D-SnS_2 NSs was sonicated and dispersed in 1.0 mL of ethanol. After the dispersion was uniform, 200 μL of the dispersion was taken out to spread the 3D-SnS_2 NSs on the surface of the IDE by a spin coater at room temperature. The spin protocol was 10 s at low speed (400 rpm) and 20 s at a high speed (2000 rpm). Finally, the IDEs uniformly covered with 3D-SnS_2 NSs were obtained and dried under vacuum at 80 °C for 2 h.

RESULTS AND DISCUSSION

Preparation and Structural Characterization of 3D-SnS_2 NSs and 3D-SnS_2 NSs/IDEs. To verify that the 3D-SnS_2 NSs formed the microscopic morphology of the stacked aggregates, the characterizations were first performed by scanning electron microscopy (SEM) and transmission electron microscopy (TEM). Figure 1a−c shows typical SEM and TEM images of some 1−2 μm 3D-SnS_2 NS irregular aggregates embedded with stacked hexagonal nanosheets with a surface width of about 500 nm. By further observing the edge of 3D-SnS_2 NSs, it was found that the hexagonal SnS_2 nanosheets are a multilayered structure (Figure 1d) with a total thickness of about 8.5 nm, the monolayer of which is about 0.6 nm, and a series of layers were about 14. Otherwise, the high-resolution TEM image (HRTEM; Figure 1e) along the (001) zone axis exhibits clear three diffraction fringes at different orientations between which the maximum angle is 65°, corresponding to the (010), (1-10), and (100) lattice plane of hexagonal SnS_2 with the same interplanar spacing of 0.315 nm. The corresponding selected area electron diffraction (SAED) pattern (Figure S1a) shows clear and bright hexagonal diffraction points along the (001) zone axis, indicating that the SnS_2 NSs with high-quality single-crystal properties exhibit high crystallinity. The hexagonal crystal structure of SnS_2 NSs

https://doi.org/10.1021/acs.analchem.2c02010
Anal. Chem. 2022, 94, 9487−9495

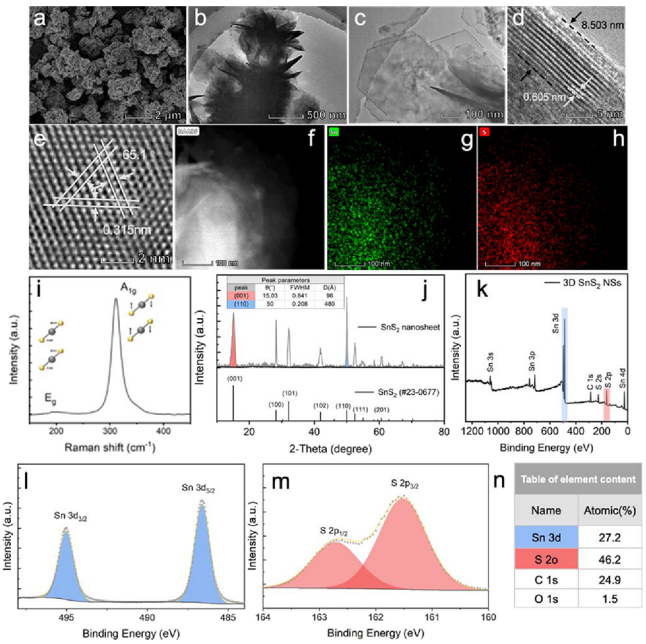

Figure 1. (a) SEM image of 3D-SnS_2 NSs. (b, c) TEM images of 3D-SnS_2 NSs (dotted line in panel (c): edge of the stacked nanosheets). (d) Cross-sectional TEM image along the edge (white: the thickness of the monolayer SnS_2 nanosheet; black: the thickness of the multilayer SnS_2 nanosheet). (e) High-resolution TEM image of nanosheets in plane view. (f) TEM image of 3D-SnS_2 NSs in the dark field. Elemental mapping images of (g) Sn and (h) S. (i) Raman spectra of 3D-SnS_2 NSs. (j) XRD pattern of the 3D-SnS_2 NSs and corresponding PDF card [inset: comparison of peak parameters of (001) and (110)]. (k) XPS survey spectra of 3D-SnS_2 NSs. High resolutions of (l) Sn 3d and (m) S 2p spectra. (n) Comparison of the element content.

indicates that the exposed top and bottom surfaces of SnS_2 were (001) crystal planes. The thickness of 3D-SnS_2 NSs after exfoliation (in low-power <50 W) was measured by atomic force microscopy (AFM). As observed in Figure S1b,c, the exfoliated SnS_2 nanosheets were mainly distributed in two sizes. The height of large portions above the mica plate is less than 1.5 nm with a surface width of 50 nm, which is the single or double layers of SnS_2 peeled off owing to the destruction of interlayer van der Waals forces. When measuring the height profile along four bright areas that is over 200 nm, the height change is about 10 nm between nanosheets and the substrate, suggesting similar results with those of TEM. Since the low power ultrasonication only destroys the van der Waals force, it can be concluded that the SnS_2 nanosheet cluster indeed consists of hexagonal SnS_2. Mapping analysis and energy-dispersive X-ray spectroscopy (EDS) characterization were used to investigate the elemental composition and content of 3D-SnS_2 NSs. As shown in Figure 1f–h, S and Sn elements were evenly distributed in the SnS_2 NS structure. Among them, the molar ratio of the S and Sn (S/Sn) was about 1.94 (Figure S1d), indicating that the hexagonal SnS_2 nanosheets with S vacancies were classical n-type semiconductors.[26]

To confirm the crystal polytype of 3D-SnS_2 NSs, Raman characterization was performed. As shown in Figure 1i, there are two characteristic peaks located at 311.6 and 203.4 cm^{-1}, corresponding to the A_{1g} mode (out-of-plane vibration) and E_g mode (in-plane vibration) attributed to 2H-SnS_2, respectively. In addition, the crystallographic structure of the 3D-SnS_2 NSs was determined by powder X-ray diffraction (XRD; Figure 1j). The positions of the diffraction peaks matched well to the standard card (JCPDS #23-0677) of the hexagonal phase of SnS_2. According to the Scherrer equation, the crystallite sizes of the (001) plane and (110) plane were 9.5 and 43 nm, respectively, which correspond to the thickness and width of the SnS_2 nanosheets. In addition, it could be estimated that the single SnS_2 nanosheet was formed by the superposition of about 16 monolayers according to the calculation formula ($N_L = \frac{D_{hkl}(001)}{C}$), in which N_L is the number of layers, D_{hkl} (001) is the crystallite size of SnS_2 on the (001) plane, and C is the lattice constant of SnS_2 in the c-axis direction, approximately 5.9 Å. Compared with SnS_2 nanosheets synthesized by CVD

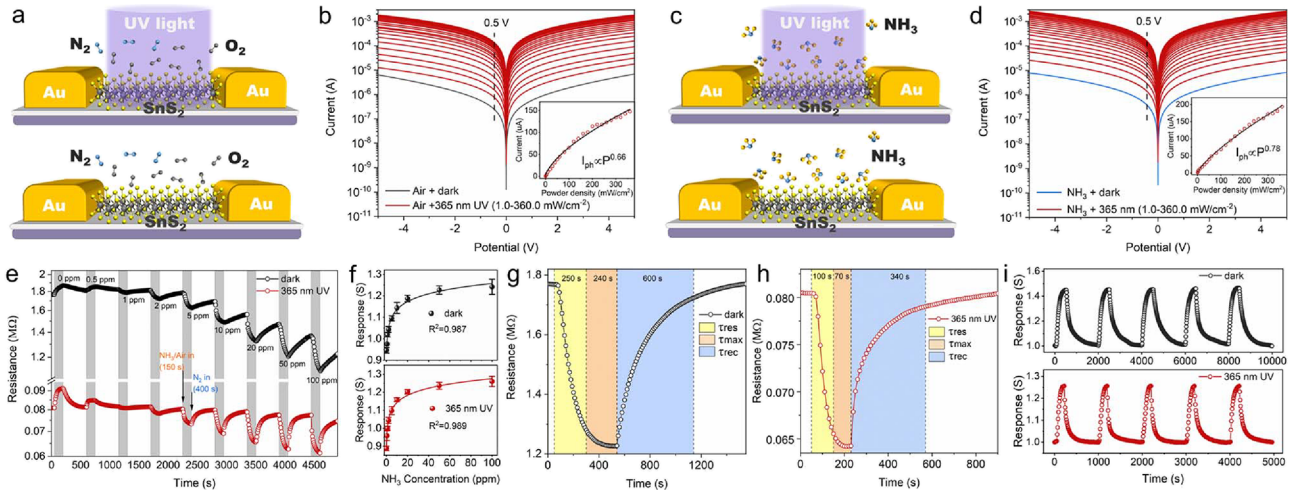

Figure 2. Photoelectric responses of the 3D SnS_2/IDEs under different working conditions at room temperature. Schematic diagrams of 3D SnS_2/IDEs and corresponding I–V characteristics in (a, b) air and in (c, d) NH_3 atmosphere under darkness and at 365 nm UV (inset: photocurrent as a function of illumination intensity from 1.0 to 360 mW/cm^2 at 0.5 V bias voltage). (e) Dynamic response curves of 3D SnS_2/IDEs for NH_3 response at 0–100 ppm under darkness and 365 nm UV light. (f) Corresponding response S of 3D-SnS_2 NSs/IDEs as a function of NH_3 concentration (error bars are 95% confidence intervals for three measurements). Dynamic response curves of 3D SnS_2/IDEs to 100 ppm NH_3 (g) in the dark and (h) at 365 nm UV. (i) Repeated dynamic responses of 3D SnS_2/IDEs for 100 ppm NH_3.

https://doi.org/10.1021/acs.analchem.2c02010
Anal. Chem. 2022, 94, 9487–9495

methods,[27] the intensity of the characteristic peak of the (001) plane was significantly reduced, which was attributed to the strong shrinkage of the (001) plane with preferential orientation, thereby forming nanosheets with fewer layers. The above results are consistent with the analysis of TEM characterization, which proves that the host of 3D-SnS_2 NSs is few-layered SnS_2 nanosheets. Simultaneously, the element valence states of 3D-SnS_2 NSs were determined by X-ray photoelectron spectroscopy (XPS) characterization. The characteristic peaks of Sn and S can be clearly observed in Figure 1k. The Sn peaks were located at 495.1 and 486.45 eV (Figure 1l), which were Sn $3d_{3/2}$ and Sn $3d_{5/2}$, respectively. The S peaks at 162.65 and 161.55 eV corresponded to S $2p_{1/2}$ and S $2p_{3/2}$ (Figure 1m). The Sn/S atomic ratio was around 1:1.92 (Figure 1n) with a value of less than 0.5, suggesting S vacancies in 3D-SnS_2 NSs. The results show agreement with the results of the EDS analysis (Figure S1d). The prepared 3D-SnS_2 nanosheets were further formed on the surface of IDEs by the spin-coating method to fabricate 3D-SnS_2 NSs/IDEs (Figure S2).

Performance Characterization of the UV-Assisted Gas Sensing System Based on 3D-SnS_2 NSs/IDEs. As important factors affecting the performance of the gas sensor, the working voltage and the radiation intensity must first be determined, and the gas sensing photocurrent test was carried out on the prepared 3D-SnS_2 NSs/IDEs (hereinafter referred to as the test electrode) with the photoelectric sensing test system (Scheme S1). As shown in Figure 2a,b, the photocurrent of the test electrode increased with the increasing optical power density of UV irradiation at 365 nm in air. The current is fitted to the irradiation power according to the power law dependence: $I_{ph} \propto P^{\theta}$, where P is the power density of the incident UV irradiation and I_{ph} is the photocurrent.[28] The exponent θ was fitted to 0.66 for the test electrode in the air (Figure 2b, inset). As shown in Figure 2c,d, the θ of the test electrode under a NH_3 (100 ppm) atmosphere was 0.78. The results show that the adsorption of O_2 of the air forms a surface state of adsorbed oxygen with a lower energy level and traps photo-generated carriers, the relationship between optical power and current deviates from linearity, and the photocurrent tends to be saturated. Meanwhile, the adsorption of NH_3 did not hinder the migration of photogenerated carriers. When NH_3 occupied part of the sites where O_2 was adsorbed, the trapped photogenerated electrons were released, and NH_3 as an electron donor could also increase the concentration of photogenerated carriers. Therefore, the relationship between optical power and photocurrent was almost linear with increasing θ. Further analysis suggested that high-intensity irradiation generates excess electrons, leading to O_2 re-adsorption and instantaneous carrier depletion, so a lower intensity of 5 mW/cm^2 was chosen as the excitation light power of the 365 nm UV. At the same time, at a bias voltage of 0.5 V, the curvature of the $I-V$ curve changed sharply (Figure 2b,d), labeling that the gas detection response was more pronounced at this voltage, which is the reason why 0.5 V was chosen as the operating voltage for subsequent experiments.

Next, to determine the photoelectric responses of O_2 and NH_3 measured by the test electrode, air with different NH_3 concentrations (0−100 ppm) was continuously fed into the sensing chamber for dynamic gas detection response tests. The ventilation times of the detection gas and the carrier gas were 150 and 400 s, respectively. As shown in Figure 2e,f, under the darkness state and 365 nm UV irradiation conditions, the response value S ($S = R_g/R_a$, where R_g and R_a were the resistances of the gas sensor in the target and background gases) of the test electrode to the NH_3 concentration was less than 1 when the concentration was less than 1 ppm and greater than 1 when the concentration was higher than 1 ppm. Under both test conditions, the gas-sensing responses of the test electrodes were linearly related to the logarithm of the NH_3 concentration (0−100 ppm) and the fitting coefficients R^2 were 0.987 (darkness) and 0.989 (365 nm UV illumination). The results indicate no impact on UV irradiation for the NH_3 response of the test electrodes. In contrast, the S value increased from 0.88 to 1.26 (Figure 2f) under UV irradiation, while under darkness, it increased only from 0.94 to 1.24 (Figure 2f) in the same NH_3 concentration range. For one single response cycle, in the dark state (Figure 2g), the response time (τ_{res}) and recovery time (τ_{rec}) were 250 and 600 s, respectively. After 490 s, the resistance of the test electrode was minimized. Under UV irradiation at 365 nm (Figure 2h), both τ_{res} and τ_{rec} shortened to 100 and 340 s, respectively, and the resistance decreased to a minimum after 170 s of NH_3 aeration. The results depict that UV irradiation can facilitate the gas sensor signal response faster, greatly shorten the recovery time after detection, and improve the detection efficiency of the test electrode. Stability as an important parameter was further investigated for NH_3 recognition by 3D-SnS_2 NSs/IDEs. By testing NH_3 (100 ppm) for five cycles under dark conditions and UV irradiation, it could be seen that the intensities of response peaks and response-recovery times were essentially the same in the respective cycles, showing good reproducibility (Figure 2i). These results demonstrate that, under a 365 nm UV irradiance of 5 mW/cm^2 and a working voltage of 0.5 V, the response signal of the test electrode fluctuates slightly, which can be considered as the optimal working voltage and light intensity.

Mechanistic Investigation of the UV-Assisted Gas Sensor of 3D-SnS_2 NSs/IDEs. To more systematically understand the essential mechanism of the UV-assisted gas sensor with improved performance, further investigations are needed to explore the difference in the O_2 and NH_3 adsorption exhibited by the SnS_2 electrodes using first-principles DFT for the theoretical analysis (Figures S3−S6 and Table S1). The electron transfer path diagram at the SnS_2 electrode surface before and after the adsorption of O_2 and NH_3 is drawn (Figure 3). Since SnS_2 is an intrinsic n-type semiconductor, the

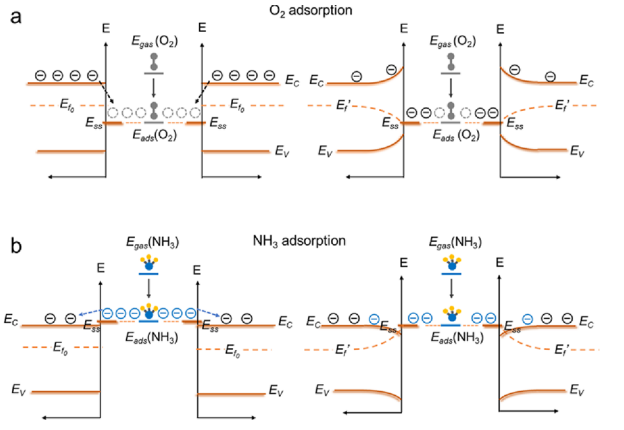

Figure 3. Schematic representation illustrating (a) the O_2 and (b) NH_3 adsorption mechanism.

https://doi.org/10.1021/acs.analchem.2c02010
Anal. Chem. 2022, 94, 9487−9495

charge carriers are electrons and the Fermi level is close to the bottom of the conduction band (CB). The Fermi level on the surface of SnS_2 is much lower than that in its interior when O_2 is adsorbed as an electron acceptor (Figure 3a), so the electrons in the CB are more inclined to enter the oxygen-adsorbed surface state of the low Fermi surface. Then, the electron concentration decreases, causing the overall Fermi level of SnS_2 to decrease while the energy level of the adsorbed surface state increases. When the adsorption and desorption of O_2 reach equilibrium (in electron transfer equilibrium), the absorbed oxygen-related surface states are at the same level as the Fermi level of SnS_2. With regard to the localization of the electrons in the surface state of adsorbed oxygen on the SnS_2 surface, a charge depletion layer is generated on the surface and the built-in electric field bends the CB upward, resulting in a higher potential barrier to be crossed when electron carriers migrate between different 3D-SnS_2 NSs, manifesting macroscopically as a decrease in the overall SnS_2 conductivity. When NH_3 is adsorbed as an electron donor (Figure 3b), the Fermi level on the SnS_2 surface is higher than that on the interior, and the electrons of the adsorbed ammonia-related surface states are injected into the CB, thereby increasing the carrier concentration and the Fermi level of SnS_2. The energy level of the adsorbed ammonia-related surface states decreases. The surface state with adsorbed ammonia is at the same level as the SnS_2 Fermi level when the equilibrium of NH_3 adsorption is reached. Since the delocalization at the SnS_2 surface from the electrons of the adsorbed NH_3 leads to a charge accumulation layer and causes the reverse built-in electric field to bend down the CB at the surface, this means that there is a lower energy barrier to cross during electron transition, thereby accelerating electron migration between the SnS_2 NSs. Additionally, electron injection by adsorbed NH_3 also increases the entire carrier concentration, which macroscopically manifests as an increase in the conductivity of SnS_2.

In addition, the conductivity changes of 3D-SnS_2 NSs induced by UV irradiation were further considered. Here, the 3D-SnS_2 NS thin-film field-effect transistor (FET) device underwent explication of the transfer characteristics in the atmosphere at room temperature under darkness and UV irradiation. As shown in Figure 4a, with the drain-source voltage constant, the drain-source current increased with the gate voltage, indicating that the device belongs to a classical n-type FET. The effective carrier mobility (μ_{eff}) of 3D-SnS_2 NS films can be calculated using the following formula:[29]

$$\mu_{eff} = \frac{dI_{SD}}{dV_G} \cdot \frac{Lh}{Z\epsilon\epsilon_0 V_{SD}}$$

Here, I_{SD} is the source-drain current of the FET, V_G is the gate voltage, L is the electrode length (3 mm), and ϵ and ϵ_0 are the relative permittivity of SiO_2 and vacuum permittivity (8.86 $\times 10^{-12}$ F/m).[30] h is the thickness of the SiO_2 layer (300 nm), Z is the source-drain spacing (100 μm), and V_{SD} is the source-drain voltage (5 V). The effective carrier mobility was calculated to be 82.7 $cm^2/(V{\cdot}s)$ in the dark state at a cutoff voltage of about 5 V, indicating that the device exhibited enhanced n-type semiconductor transfer characteristics. The internal carriers of SnS_2 were depleted, so a forward gate voltage was required to counteract the internally generated positive charge when the FET was turned on,[31] which could be blamed on a large amount of O_2 adsorption on the SnS_2 surface in the darkness. With the 365 nm UV irradiation, the

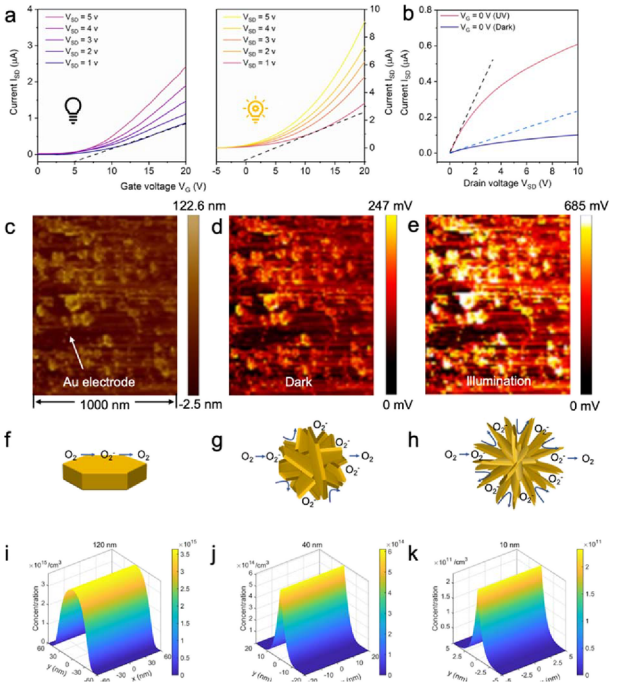

Figure 4. (a) Relationship between I_{SD} and V_G for V_{SD} of 3D-SnS_2 NSs ranging from 1 to 5 V without (left) and with UV illumination (right). (b) I_{SD}–V_{SD} curves of 3D-SnS_2 NSs without and with UV illumination at 0 V gate voltage. (c) Topography image of SnS_2 nanosheets attached to a metal electrode and corresponding surface potential maps of nanosheets (d) in the dark and (e) under 365 nm UV illumination. Schematic diagram of the stacking structure of 3D-SnS_2 NSs assembled by (f) 120 nm, (g) 40 nm, and (h) 10 nm nanosheets with adsorbed oxygen. Distributions of the carrier concentration in multilayer SnS_2 with (i) 120 nm, (j) 40 nm, and (k) 10 nm thickness in the dark.

cutoff voltage decreased to −1 V and the effective carrier mobility increased to 155.2 $cm^2/(V{\cdot}s)$. This was promoted by UV irradiation to generate abundant photoelectrons inside the 3D-SnS_2 NSs and initiate O_2 desorption on the SnS_2 surface, thus decreasing the cutoff voltage and enhancing the carrier migration between SnS_2 NSs. The conductivity (σ) of the electrode in darkness and UV exposure could be calculated to be about 6×10^{-7} and 2.5×10^{-5} S/cm (Figure 4b), respectively, which was based on the formula $\sigma = \sum_j q n_j \mu_j = q n_{eff} \mu_{eff}$. Furthermore, the μ_{eff} of the 3D-SnS_2 NSs increased by 2 orders of magnitude from 4.5×10^{10} to $1.0 \times 10^{12}/cm^3$ with UV irradiation, suggesting that reducing O_2 adsorption at the electrode surface effectively boosts the carrier density. In summary, the surface O_2 adsorption decreases, and the conductivity of 3D-SnS_2 NSs increases when UV irradiation is present.

As evident from the characterization of thin-film FETs, surface O_2 adsorption negatively impacts the conductivity of the 3D-SnS_2 NS electrode. In light of this, the morphology and surface potential were characterized by AFM with a xenon lamp light source considering the difference in the surface O_2 adsorption of different intrinsic structures. The height of prepared 3D-SnS_2 NSs was about 120 nm (Figure 4c). The surface potential of the Au film was about −105 mV in a dark environment, which was used as the zero point of the contact potential difference to calibrate the surface potential of 3D-SnS_2 NSs. As pointed out in Figure 4d,e and Figure S7, the surface potential of 3D-SnS_2 NSs is about 247 mV in the dark.

https://doi.org/10.1021/acs.analchem.2c02010
Anal. Chem. 2022, 94, 9487−9495

Taking the potential (0 mV) of a Au film with a work function of 5.1 eV as a reference,[32] it could be obtained that its work function was approximately 4.853 eV. The surface potential of 3D-SnS_2 NSs increased and stabilized at 685 mV with the stepwise increase in UV illumination power. This result was attributed to the gradual increase in the photogenerated hole concentration caused by the enhancement power of the UV irradiation, which accelerated the desorption of negatively charged O_2 at the SnS_2 surface. The increased surface potential over the process of UV illumination was defined as surface photovoltage (SPV). The SPV increased and tended to 438 mV in the last stage, demonstrating that the complete desorption of surface-adsorbed O_2 and the built-in potential barrier disappears. The SPV at this point was about 4.415 eV, which could be used to assess the work function of 3D-SnS_2 NSs without O_2 adsorption. The work function change ($\Delta\Phi$) of 3D-SnS_2 NSs under the dark and UV irradiation could be approximated as the $\Delta\Phi$ of SnS_2 caused by O_2 adsorption in the darkness. The surface carrier concentration of 3D-SnS_2 NSs was $1.63 \times 10^8/cm^3$ according to the calculation (the calculation process is in the Supporting Information). Under UV irradiation, the distance between the surface conduction band and the Fermi level (*E*S C−E_F) gradually decreased to 0.165 eV with increasing irradiation intensity, and the carrier concentration returned to $3.72 \times 10^{15}/cm^3$. This result demonstrated that O_2 adsorption could significantly reduce the surface carrier concentration of 3D-SnS_2 NSs, thereby severely limiting carrier transfer between SnS_2 nanosheets, and was consistent with the characterization analysis of the thin-film FET.

Considering that 3D-SnS_2 NSs were assembled from few-layered SnS_2 nanosheets, the relationship between O_2 adsorption sites and the finite size (thickness) of nanosheets aroused our interest. The 3D-SnS_2 NSs tended to be nanoblocks with a thickness of 120 nm (Figure 4f), indicating that the O_2 adsorption sites were only on the top and bottom surfaces. When the thickness was reduced to 40 nm (Figure 4g), the 3D-SnS_2 NSs were formed by stacking a small number of nanoblocks with increasing surface O_2 adsorption sites. Reduced further to 10 nm (Figure 4h), the 3D-SnS_2 NSs were visualized as a flower-like structure with a substantial number of O_2 adsorption sites per unit space. On the other way, surface potential analysis proved that O_2 adsorption would decrease the surface carrier concentration. In the situation where the size was smaller than the depletion region width (W_{crit}) caused by O_2 adsorption, the distance between the CB inside the semiconductor and the Fermi level (*E*B C−E_F) improved and further depleted the charge carriers inside the material.[33] Therefore, the 3D electrostatic field constructed the space charge model of SnS_2 NSs (10, 40, and 120 nm) and simulated their internal potential and carrier concentration distribution. The W_{crit} generated by O_2 adsorption was derived at 54.2 nm by substituting the measured SPV (0.438 eV) into the simulation equation. The voltage gradually approached 0 with closer to the center, and the carrier concentration gradually increased. The *E*B C−E_F of O_2 adsorption in the dark was equal to the SPV (0.438 V) in the 120 nm SnS_2 nanoblocks (Figure 4i and Figure S8a). At this time, the central voltage was 0, and the central carrier concentration reached $3.72 \times 10^{15}/cm^3$. When the thicknesses of the nanosheets were 40 nm (Figure 4g and Figure S8b) and 10 nm (Figure 4k and Figure S8c), the central voltages were −0.047 and −0.25 V, respectively, and the internal carrier concentrations decreased by several orders of magnitude to 6.11×10^{14} and $2.32 \times 10^{11}/cm^3$, respectively. For an *E*S C−*E*B of 0.438 eV, the surface electric field intensity was 1.89×10^7 V/m with 120 nm SnS_2 and the surface charge density (Q_S) was 2.86×10^{-6} C/cm^2 according to Gauss's theorem: $Q = \epsilon\epsilon_0 \frac{dV}{dr}|r_0$. At the same time, it could be known that the density of the adsorbed oxygen-related surface states (n_{ss}) formed in SnS_2 was calculated by the formula $n_{ss} = \frac{Q_S}{e}$ to be $1.78 \times 10^{14}/cm^2$. When the thicknesses were reduced to 40 and 10 nm with the surface potential remaining unchanged, their surface electric fields gradually decreased to 1.06×10^7 and 5.66×10^6 V/m and the corresponding energies of surface state (E_{ss}) were 9.97×10^{13} and $5.30 \times 10^{13}/cm^2$. Further analysis verified that, when the W_{crit} generated by O_2 adsorption was less than half the thickness of SnS_2 (60 nm), the SPV generated by UV irradiation was regarded as *E*S C−*E*B C, resulting in no effect on the carriers inside the CB. Conversely, if the W_{crit} was greater than half the thickness of SnS_2 (20 or 5 nm), then part of *E*S C−*E*B C was converted to *E*B C−E_F. At this time, *E*S C−*E*B C decreased, the surface electric field strength of SnS_2 reduced, and the surface charge density decreased. However, the increase in *E*B C−E_F caused rapid depletion of internal carriers, and the n_{ss} of O_2 adsorption on the thinner SnS_2 surface decreased under the same SPV to have a larger impact on the total carriers. From these results, it could be concluded that, when O_2 was adsorbed on a thinner SnS_2 ($<W_{crit}$) in the same n_{ss}, the SPV decreased and the work function of SnS_2 increased due to the lower surface electric field strength, which meant that the holes generated by the same UV irradiation intensity had less ability to destroy the O_2 adsorption on the surface. Therefore, the electron-withdrawing effect of O_2 adsorption per unit was enhanced, and the SnS_2 became more sensitive to the adsorption and desorption of O_2.

As a summary, the adsorption behavior of adsorbed gas molecules (O_2 and NH_3) on the surface of SnS_2 nanosheets was studied using the classical Wolkeinstein semiconductor surface gas molecule chemisorption model.[34,35] By meliorating the model and adding the UV irradiance factors, the reasons for the improved responsivity of O_2 and NH_3 molecular sensors with UV were clarified. With the parameters discussed above, the surface space charge models of SnS_2 under O_2 and NH_3 were simulated to delineate the electron transfer pathways of SnS_2/IEDs under UV irradiation in the presence of target gas molecules (Figure 5). When SnS_2/IEDs were

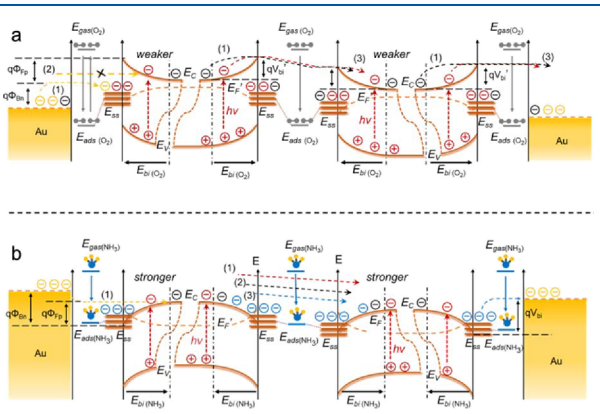

Figure 5. Schematic illustration of the mechanism of (a) O_2 and (b) NH_3 adsorption on the surface of SnS_2/IDEs under UV irradiation.

https://doi.org/10.1021/acs.analchem.2c02010
Anal. Chem. 2022, 94, 9487−9495

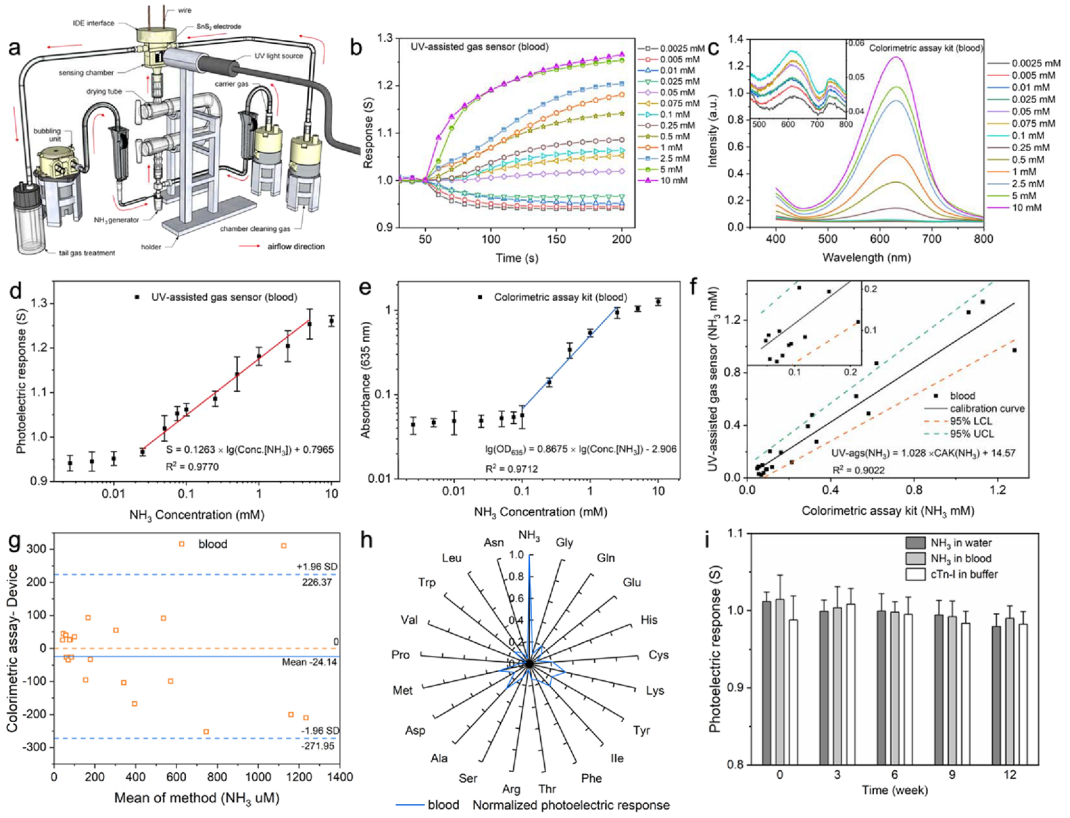

Figure 6. (a) Schematic depiction of UV−AGS design. (b) Photoelectric response vs time trace and (c) absorbance vs time trace for NH_3 measurement in a whole blood sample. The linear relationship showed in (d) the UV-assisted gas sensor and (e) the colorimetric assay kit between the signal response and the logarithm of the NH_4Cl concentration (0.0025−10,000 μM) for NH_3 measurement in a whole blood sample. (f) Correlative analysis of ammonia measurement and (g) Bland−Altman plot of two methods for NH_3 measurement in a whole blood sample. (h) Selectivity test of UV−AGS for NH_3 measurement in a whole blood sample (NH_3: 100 μM, each amino acid: 1 mM). (i) Stability test of UV−AGS devices for NH_3 measurement in the (black) water sample and in the (gray) whole blood sample and cTnI measurement in the (white) buffer sample in the long-term storage (error bars are 95% confidence intervals for three measurements).

exposed to UV illumination, the addition of photogenerated electrons/holes rapidly increased the carrier concentration, and the photogenerated holes reacted with the adsorbed oxygen under the built-in electric field further leading to the oxygen desorption. Afterward, the original adsorption equilibrium was broken, and both O_2 and NH_3 in the mixed gas had equal opportunities to combine with SnS_2 surface adsorption sites. Since the larger adsorption energy of NH_3 makes it more dominant in the adsorption process on the surface of SnS_2, it leads to improved NH_3 responsivity. At the same time, O_2 in the mixed gas could also be reabsorbed on the SnS_2, and the Fermi level of SnS_2 was increased by light compared to the dark state. In this case, when the O_2 concentration was further increased, the responsiveness of O_2 reabsorption was also improved compared to darkness. This difference in response was further amplified under UV illumination due to the difference between O_2 and NH_3 as electron donors and electron acceptors. In addition, the Schottky barrier formed by the Au electrode and SnS_2 could also regulate the migration of carriers. Under UV irradiation, the Schottky barrier increased by O_2 adsorption while the NH_3 condition decreased the barrier, consistent with the condition that the interval barrier between SnS_2 was exceeded. Therefore, there appears to be a promising analysis of O_2 and NH_3 in the mixed gas with UV illumination.

Construction and Performance Exploration of the Bioanalytical Platform. To realize the idea of constructing the contactless photoelectrochemical biosensor based on the test electrode, an integrated UV-assisted gas sensing (UV−AGS) device (Figure 6a and Figure S9) was utilized to analyze the NH_4Cl standard sample (hereinafter referred to as the NH_3 standard) as a feasibility test. As presented in Figure S10, associations between the photoelectric response (S) and logarithm of the NH_3 concentration in the NH_3 standard within a specified range (5−5000 μM) were assessed using a linear regression of the fitted equation S = 0.1420 lg(Conc.[NH_3]) + 0.7431 (n = 3, R^2 = 0.9804). The limit of detection (LOD) for this method was 10.1 μM with a relative standard deviation (RSD) ranging from 1.2 to 2.5%.

Based on these observations, the UV−AGS apparatus further performed blood ammonia analysis of NH_3 measurements in whole blood samples (hereinafter referred to as NH_3 whole blood samples) and the gas-phase immunoassay for cTnI dissolved in buffer solution (hereinafter referred to as cTnI buffer). To further validate the analytical performance of the UV−AGS device, the response curves of the UV−AGS method (Figure 6b) and the commercial assay kit in colorimetry (Figure 6c) were plotted for different sample concentrations. There was a good linear relationship between the S and NH_3 concentration (25−5000 μM) in the whole blood sample with the UV−AGS device and was determined by a fitted regression equation of S = 0.1263 lg(Conc.[NH_3]) + 0.7965 (n = 3, R^2 = 0.9770) with an LOD of 29.5 μM, and the RSD range was between 0.9 and 1.3% (Figure 6d). The LOD with lower

https://doi.org/10.1021/acs.analchem.2c02010
Anal. Chem. 2022, 94, 9487−9495

sensitivity may be due to the influence of non-specific substances such as fibrinogen in NH_3 whole blood samples on the detection results, but its analytical performance can still match the clinical practice. As to the colorimetric method (Figure 6e), the NH_3 concentration (100−2500 μM) in the NH_3 whole blood samples showed a good linear relationship with the OD_{635} of the test solution. The fitted regression equation is $\lg(OD_{635}) = 0.8675 \lg(\text{Conc.}[NH_3]) - 2.906$ (n = 3, $R^2 = 0.9712$) with the LOD in 141.6 μM, and the RSD range is between 5.3 and 7.6%. It is noted that the LOD of the colorimetric detection is much higher than that of the UV−AGS device in blood ammonia analysis, indicating the presence of nonspecific substances in the whole blood samples that interfere with the colorimetric reaction. Therefore, colorimetry is unsuitable for the direct blood ammonia analysis with whole blood samples. To examine the consistency of the UV−AGS device and the commercial kit, a series of NH_3 whole blood samples (25−1000 μM) were tested using two methods to plot a calibration curve in variables of the test results. Figure 6f represents the slope of the UV−AGS method, and the commercial kit for NH_3 whole blood samples is 1.028 with the Pearson correlation coefficients of 0.9524 (p < 0.845) and 0.9799 (p < 0.914), indicating that the two methods exhibit good correlation in the tested concentration range. To examine the consistency analysis among continuous variables, Bland−Altman analysis was performed for the two methods. As shown in Figure 6g, for the detection of NH_3 whole blood samples, the average deviation of the two methods was −24.14 μM and most of the method differences of the samples were all within two SD. The analysis results became positively biased at low concentrations by the UV−AGS device and slightly positively biased by the colorimetric kit at high concentrations. In general, good consistency was observed between the UV−AGS method and the commercial kit in analyzing the test samples. In addition, the agreement of the two methods for NH_3 standard and cTnI buffer samples has been also carefully analyzed (Figures S11 and S12) and also shows good consistency. Furthermore, the deviation of the test value and the true value of the sample concentration was explored. The parameters of the test results of the three sample groups were compared and analyzed (Table S2) to assess whether both methods reflect the authenticity of the analyte concentrations.

Considering that small molecules containing primary amines in blood also respond to the generation of signals, 20 essential amino acids were selected as interfering substances for NH_3 analysis to evaluate the specificity of the UV−AGS method. The photoelectric response of each amino acid was normalized according to the signal of NH_3. The highest responding amino acids were alanine (Ala) and lysine (Lys) with the relative response values of only 0.223 and 0.341, respectively (Figure 6h), showing that the UV−AGS device had good specificity for blood ammonia analysis. The specificity of detection of NH_3 standards and cTnI buffer for the UV−AGS device is summarized in Figure S13. To investigate the test stability of the UV−AGS device, 3D-SnS_2 NSs/IDEs of different storage periods (0−12 weeks) were selected to analyze NH_3 standards, NH_3 whole blood samples, and cTnI buffer samples in the same concentration (Figure 6i). The photoelectric response decreased to 96.8 and 97.6% after 12 weeks of storage in the concentration determination of NH_3 standards and whole blood samples with the maximum values in the RSD of the test results of 2.2 and 3.1%, respectively. In the cTnI buffer test, the response was weakened to 99.4% of baseline at 12 weeks, with a maximum RSD of 3.2% throughout the test. The above results indicate that there is stable signal output for both blood ammonia analysis and cTnI immunoassay based on the UV−AGS device, which is benefited from the fact that the 3D-SnS_2 NS/IDE electrodes are stored in the vacuum after each test has been dried to avoid moisture air for a long time.

CONCLUSIONS

In this work, the UV-assisted gas sensor based on 3D-SnS_2 NSs was developed, which could be used for direct blood ammonia detection in small-volume whole blood samples and cTnI immunoassays. 3D-SnS_2 NSs/IDEs were fabricated as gas sensing electrodes for O_2 and NH_3 detection obtained by simple water bath deposition and spin coating methods. Analysis tools for theoretical calculations such as three-dimensional electrostatic field simulations and first-principles DFT allow a deeper perspective on the occurrence of gas sensing at the electrodes. The process of signal amplification by UV irradiation and the response to O_2 and NH_3 of various 3D-SnS_2 NS structures were further elucidated. The UV−AGS obtained by 3D printing was designed from the guidance of gas sensing principles. It is a device that separates the response identification process and the signal generation process, which can largely avoid the damage to the response electrode, simplify the design of the semiconductor interface, and also achieve a certain degree of portability and high sensitivity.

ASSOCIATED CONTENT

Supporting Information

The Supporting Information is available free of charge at https://pubs.acs.org/doi/10.1021/acs.analchem.2c02010.

Experimental section, model information, calculation process, analysis performance, consistency analysis, and additional schemes, figures, and tables (PDF)

AUTHOR INFORMATION

Corresponding Author

Dianping Tang − *Key Laboratory for Analytical Science of Food Safety and Biology (MOE & Fujian Province), Department of Chemistry, Fuzhou University, Fuzhou 350108, People's Republic of China*; orcid.org/0000-0002-0134-3983; Phone: +86-591-2286 6125; Email: dianping.tang@fzu.edu.cn; Fax: +86-591-2286 6135

Authors

Lingting Huang − *Key Laboratory for Analytical Science of Food Safety and Biology (MOE & Fujian Province), Department of Chemistry, Fuzhou University, Fuzhou 350108, People's Republic of China*

Guoneng Cai − *Key Laboratory for Analytical Science of Food Safety and Biology (MOE & Fujian Province), Department of Chemistry, Fuzhou University, Fuzhou 350108, People's Republic of China*

Ruijin Zeng − *Key Laboratory for Analytical Science of Food Safety and Biology (MOE & Fujian Province), Department of Chemistry, Fuzhou University, Fuzhou 350108, People's Republic of China*

Zhichao Yu − *Key Laboratory for Analytical Science of Food Safety and Biology (MOE & Fujian Province), Department of Chemistry, Fuzhou University, Fuzhou 350108, People's Republic of China*

https://doi.org/10.1021/acs.analchem.2c02010
Anal. Chem. 2022, 94, 9487−9495

Complete contact information is available at:
https://pubs.acs.org/10.1021/acs.analchem.2c02010

Author Contributions

[ξ]L.H. and G.C. contributed equally.

Notes

The authors declare no competing financial interest.

■ ACKNOWLEDGMENTS

We gratefully acknowledge the financial support from the National Natural Science Foundation of China (21874022 and 21675029).

■ REFERENCES

(1) Gao, Y.; Zeng, Y.; Liu, X.; Tang, D. *Anal. Chem.* **2022**, *94*, 4859−4865.
(2) Yu, Z.; Gong, H.; Xu, J.; Li, Y.; Zeng, Y.; Liu, X.; Tang, D. *Anal. Chem.* **2022**, *94*, 3418−3426.
(3) Yu, Z.; Gong, H.; Li, Y.; Xu, J.; Zhang, J.; Zeng, Y.; Liu, X.; Tang, D. *Anal. Chem.* **2021**, *93*, 13389−13397.
(4) Shu, J.; Tang, D. *Anal. Chem.* **2020**, *92*, 363−377.
(5) Lv, S.; Zhang, K.; Zhu, L.; Tang, D. *Anal. Chem.* **2020**, *92*, 1470−1476.
(6) Yang, S.; Jiang, C.; Wei, S. *Appl. Phys. Rev.* **2017**, *4*, No. 021304.
(7) Majhi, S. M.; Mirzaei, A.; Kim, H. W.; Kim, S. S.; Kim, T. W. *Nano Energy* **2021**, *79*, No. 105369.
(8) Chizhov, A.; Rumyantseva, M.; Gaskov, A. *Nanomaterials* **2021**, *11*, 892.
(9) Espid, E.; Taghipour, F. *Crit. Rev. Solid State Mater. Sci.* **2017**, *42*, 416−432.
(10) Zeng, R.; Lian, K.; Su, B.; Lu, L.; Lin, J.; Tang, D.; Lin, S.; Wang, X. *Angew. Chem., Int. Ed.* **2021**, *60*, 25055−25062.
(11) Huang, Y.; Sutter, E.; Sadowski, J. T.; Cotlet, M.; Monti, O. L. A.; Racke, D. A.; Neupane, M. R.; Wickramaratne, D.; Lake, R. K.; Parkinson, B. A.; Sutter, P. *ACS Nano* **2014**, *8*, 10743−10755.
(12) Xu, L.; Zhang, P.; Jiang, H.; Wang, X.; Chen, F.; Hu, Z.; Gong, Y.; Shang, L.; Zhang, J.; Jiang, K.; Chu, J. *Small* **2019**, *15*, 1904116.
(13) Fan, C.; Liu, Z.; Yuan, S.; Meng, X.; An, X.; Jing, Y.; Sun, C.; Zhang, Y.; Zhang, Z.; Wang, M.; Zheng, H.; Li, E. *ACS Appl. Mater. Interfaces* **2021**, *13*, 35889−35896.
(14) Zhan, S.; Zheng, L.; Xiao, Y.; Zhao, L.-D. *Chem. Mater.* **2020**, *32*, 10348−10356.
(15) Yan, W.; Lv, C.; Zhang, D.; Chen, Y.; Zhang, L.; Ó Coileáin, C.; Wang, Z.; Jiang, Z.; Hung, K. M.; Chang, C. R.; Wu, H. C. *ACS Appl. Mater. Interfaces* **2020**, *12*, 26746−26754.
(16) Wan, Q.; Chen, X.; Gui, Y. *ACS Omega* **2020**, *5*, 8919−8926.
(17) Eom, T. H.; Cho, S. H.; Suh, J. M.; Kim, T.; Lee, T. H.; Jun, S. E.; Yang, J. W.; Lee, J.; Hong, S.-H.; Jang, H. W. *J. Mater. Chem. A* **2021**, *9*, 11168−11178.
(18) Xiong, Y.; Xu, W.; Ding, D.; Lu, W.; Zhu, L.; Zhu, Z.; Wang, Y.; Xue, Q. *J. Hazard. Mater.* **2018**, *341*, 159−167.
(19) Yin, S.; Zhao, X.; Jiang, E.; Yan, Y.; Zhou, P.; Huo, P. *Energy Environ. Sci.* **2022**, *15*, 1556−1562.
(20) Zuo, Y.; Liu, Y.; Li, J.; Du, R.; Yu, X.; Xing, C.; Zhang, T.; Yao, L.; Arbiol, J.; Llorca, J.; Sivula, K.; Guijarro, N.; Cabot, A. *ACS Appl. Mater. Interfaces* **2019**, *11*, 6918−6926.
(21) Zhu, Q.; Gu, D.; Liu, Z.; Huang, B.; Li, X. *Sens. Actuators, B* **2021**, *349*, No. 130775.
(22) Gu, D.; Wang, X.; Liu, W.; Li, X.; Lin, S.; Wang, J.; Rumyantseva, M. N.; Gaskov, A. M.; Akbar, S. A. *Sens. Actuators, B* **2020**, *305*, No. 127455.
(23) Barsotti, R. *J. Pediatr.* **2001**, *138*, S11−S20.
(24) Veltman, T. R.; Tsai, C. J.; Gomez-Ospina, N.; Kanan, M. W.; Chu, G. *ACS Sens.* **2020**, *5*, 2415−2421.
(25) van der Linden, N.; Wildi, K.; Twerenbold, R.; Pickering, J.; Than, M.; Cullen, L.; Greenslade, J.; Parsonage, W.; Nestelberger, T.; Boeddinghaus, J.; Badertscher, P.; Gimenez, M.; Klinkenberg, L.; Bekers, O.; Schoni, A.; Keller, D.; Sabti, Z.; Puelacher, C.; Cupa, J.; Schumacher, L.; Kozhuharov, N.; Grimm, K.; Shrestha, S.; Flores, D.; Freese, M.; Stelzig, C.; Strebel, I.; Miro, O.; Rentsch, K.; Morawiec, B.; Kawecki, D.; Kloos, W.; Lohrmann, J.; Richards, A.; Troughton, R.; Pemberton, C.; Osswald, S.; van Dieijen-Visser, M.; Mingels, A.; Reichlin, T.; Meex, S.; Mueller, C. *Circulation* **2018**, *138*, 989−999.
(26) Shafique, A.; Samad, A.; Shin, Y.-H. *Phys. Chem. Chem. Phys.* **2017**, *19*, 20677−20683.
(27) Zhou, X.; Zhang, Q.; Gan, L.; Li, H.; Zhai, T. *Adv. Funct. Mater.* **2016**, *26*, 4405−4413.
(28) Tamalampudi, S. R.; Lu, Y. Y.; U, R. K.; Sankar, R.; Liao, C. D.; Moorthy, B.; Cheng, C. H.; Chou, F. C.; Chen, Y.-T. *Nano Lett.* **2014**, *14*, 2800−2806.
(29) Martel, R.; Schmidt, T.; Shea, H. R.; Hertel, T.; Avouris, P. *Appl. Phys. Lett.* **1998**, *73*, 2447−2449.
(30) McPherson, J.; Kim, J.-Y.; Shanware, A.; Mogul, H. *Appl. Phys. Lett.* **2003**, *82*, 2121−2123.
(31) Hong, W.-K.; Sohn, J. I.; Hwang, D.-K.; Kwon, S.-S.; Jo, G.; Song, S.; Kim, S.-M.; Ko, H.-J.; Park, S.-J.; Welland, M. E.; Lee, T. *Nano Lett.* **2008**, *8*, 950−956.
(32) Atxabal, A.; Braun, S.; Arnold, T.; Sun, X.; Parui, S.; Liu, X.; Gozalvez, C.; Llopis, R.; Mateo-Alonso, A.; Casanova, F.; Ortmann, F.; Fahlman, M.; Hueso, L. *Adv. Mater.* **2017**, *29*, 1606901.
(33) Li, G.; Meng, L.; Zhu, X.; Gao, W.; Qin, Y.; Chen, L. *Nanoscale* **2018**, *10*, 2242−2248.
(34) Wolkenstein, T. *Electronic Processes on Semiconductor Surfaces during Chemisorption*; Consultants Bureau: New York, 1991; p 444, DOI: 10.1007/978-1-4615-3656-7.
(35) Li, G.; Sun, Z.; Zhang, D.; Xu, Q.; Meng, L.; Qin, Y. *ACS Sens.* **2019**, *4*, 1577−1585.